Research

Evaluation of inversion approaches for plates based on guided waves and modal analysis

Karl-Alexander Hoppe[1] · Simon Schmid[2] · Jochen Kollofrath[2] · Steffen Marburg[1] · Christian U. Grosse[2]

Abstract

The identification of defects in plate-like structures has been successfully treated using both local guided ultrasonic waves and global modal quantities. Although there are many papers on these techniques, a lack of comparability between the two methods persists. This makes it difficult for users to identify the most appropriate method for the defect in question. This paper examines the effect of different parameterizations of a circular defect in a square aluminum plate on the system response in a case study. The measured local ultrasound signal from a propagating guided wave makes up the initial data set. The first method uses the entire waveform for the objective function of the optimization problem, while the second considers the velocity of the A_0 mode. In the third and fourth methods, the first and second global natural frequencies of the plate modeled with free-free boundary conditions are investigated. The numerical models are validated experimentally through measurements with a laser Doppler vibrometer. This results in the qualitative and quantitative evaluation of the objective functions for all parameter combinations of the defect. The recommendation to sequentially employ modal analysis and then the ultrasound procedure is made for the defect type used in this study. The data gathered on the objective functions suggests that potential joint employment of the natural frequency and ultrasound methods may increase computational efficiency. For a specific case, the methods could also complement each other in terms of challenges such as local minima.

Highlights

- Comparison of defect detection methods for plate-like structures using guided waves and global structural modes.
- Identification of advantages and limitations from the objective function values related to defect size and position.
- Modal data provides ambiguous but smooth estimates of defect properties; ultrasound yields narrowly localized minima.

✉ Karl-Alexander Hoppe, alexander.hoppe@tum.de; Simon Schmid, sim.schmid@tum.de | [1]Technical University of Munich, TUM School of Engineering and Design, Department of Engineering Physics and Computation, Chair of Vibroacoustics of Vehicles and Machines, Boltzmannstr. 15, 85748 Garching bei München, Bavaria, Germany. [2]Technical University of Munich, TUM School of Engineering and Design, Department of Materials Engineering, Chair of Non-destructive Testing, Franz-Langinger-Str. 10, 81245 Munich, Bavaria, Germany.

1 Introduction

Determining the position and size of defects by imaging constitutes one of the challenges in non-destructive testing (NDT) and structural health monitoring (SHM) [1]. Corrosion presents a common defect type that leads to a local change in the wall thickness of metal pipes and pressure vessels. Conventionally, the remaining wall thickness is determined with time-of-flight measurements of ultrasonic bulk waves. Since this is time-consuming and the structure is not always fully accessible, there is a need for more efficient approaches, see [2]. Guided waves, especially Lamb waves, are efficient approaches to both structural health monitoring [3] and non-destructive testing [4]. With guided wave tomography, the dispersion characteristics of the ultrasonic waves are utilized in order to reconstruct defects such as the change in wall thickness or delaminations in composite structures [5, 6]. Different approaches for guided wave tomography exist in the literature. They use the travel time [1] or diffraction [7] of the ultrasonic wave. Also, a hybrid approach of the previous two, called the Hybrid Algorithm for Robust Breast Ultrasound Tomography (HARBUT), exists [8]. He et al. [9] make use of the full waveform with reverse time migration. Further, the full waveform inversion (FWI) method is utilized for guided wave tomography [10]. This method is intended for imaging problems in seismic applications in geophysics. With this method, an objective function is calculated based on the whole captured signal. With this objective function, an optimization problem is solved by updating the material model [10]. In order to map the calculated velocity image to the plate thickness, dispersion thickness mapping is used for all the previously introduced methods [8].

Another method for defect detection consists of using modal parameters like eigenfrequencies. This technique is applied successfully to characterize cracks in slender structures [11]. But changes in the resonance frequencies are also linked to the thickness change in plates [12]. If the mode shapes are available as data, they offer a precise identification of the elastic material of structures such as plates [13]. In [14], strain mode shapes are used to calculate the sensitivity indices of defects in plates. When using more than one mode shape, the locations of the defects are accurately identified. In [15], defects are detected with modal analysis. A rectangular area at a fixed position with a reduced thickness serves as a defect. They investigate the relationship between the mass change through the defect and the eigenfrequencies. The authors assume that corrosion could be detected through the deduced relation. Modal analysis plays an important role in structural health monitoring. Le et al. [16] employ the modal strain energy method based on modal data to identify damage to an aluminum plate and identify mode numbers relevant to the inverse problem. Hou et al. [17] locally add mass to their structure to gain insight into the local resonance frequencies for health monitoring purposes of a truss. Park et al. [18] accomplish health monitoring of bridges experimentally by fusing local and global acceleration data. Sun et al. [19] consider the numerically obtained natural frequencies and modes of a planar structure and a truss in a Bayesian damage detection scheme. Frequency response functions are suitable for identifying the piece-wise heterogeneous Young's modulus of composite structures [20, 21]. This procedure is extended to account for continuously heterogeneous materials, which may be regarded as a generalized defect in [22].

Reviewing the literature reveals that only limited efforts have been made so far to set ultrasonic and modal approaches in relation to each other. Mengelkamp and Fritzen [23] classify plates into damaged and non-damaged using a global vibration-based method and conditionally localize the damage with ultrasonic guided waves. The considered damage categories are cracks and delaminations. Fritzen and Mengelkamp [24] perform a similar study on artificial cracks in stiffened plates. Wang and Hao [25] employ guided wave and structural vibration tests of steel beams experimentally and numerically. They find that a shared objective function is not expedient and recommend a procedure consisting of two steps, one for each testing method. Claiming to bridge between modal analysis and guided waves, Yan and Rose [26] develop a damage identification method based on operating deflection shape analysis of the steady-state response to ultrasonic excitation of an aluminum plate in the kHz order of magnitude. Ahmed et al. [27] propose the usage of a guided wave method within a global method considering structural vibrations. They study its application to identify defects in a composite wing structure using regression models.

To the authors' knowledge, methods based on guided waves and modal parameters for defect detection in plate-like structures have not yet been compared in the context of optimization problems. Furthermore, the current methods for guided wave tomography are based on the reconstruction of a velocity image and use a dispersion thickness mapping in order to calculate the plate thickness. This study introduces a method that directly changes the topography of the mesh. We focus on the advantages and restrictions of the four methods and investigate the objective function values over the defect parameters range. The results are based on simulations, while our measurements

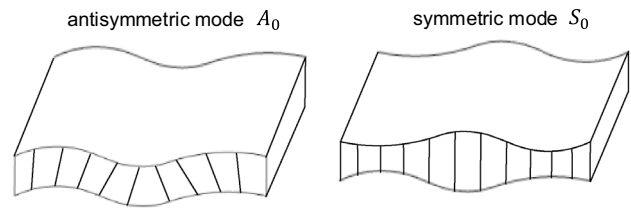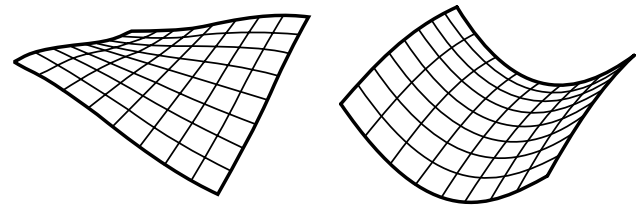**Fig. 1** Schematic display of the antisymmetric A_0 and symmetric S_0 Lamb wave modes

Fig. 2 A schematic of the first vibrational mode shape of the square plate is shown on the left, while the second mode shape is sketched on the right

serve to calibrate the simulation models. The subsequent application of an optimization algorithm should be pursued in future research. Our conclusions apply to the case study and any generalizations to other simulation setups or experimental ones with real transducers shall be conducted with care.

This paper is organized as follows: Sect. 2 covers the propagation of ultrasonic waves in plates and the latters' modal analysis. Section 3 details the simulation models and their calibration using measurements. Section 4 presents the objective functions for all methods and a strategic variation of the defect parameters. Finally, we draw some conclusions in Sect. 5.

2 Theoretical background

This section introduces the relevant basics of guided ultrasonic waves (Sect. 2.1) and modal parameters (Sect. 2.2).

2.1 Propagation of ultrasonic waves in plates

Lamb waves are guided waves propagating between two parallel boundaries [28]. They solely exhibit displacements along the propagation direction and the direction perpendicular to the plate. Waves featuring displacements in the remaining direction are referred to as shear-horizontal. In this study, only Lamb waves, where displacement is measured perpendicular to the propagation direction, are observed. For that reason, only Lamb waves will be further explained in this subsection. Lamb waves occur when longitudinal (p-) and transversal (s-) waves superimpose. Based on the boundary position (e.g. thickness of the plate) and the frequency of the ultrasonic wave, several characteristic modes occur [29]. The modes are distinguished as symmetric S_i and antisymmetric A_i modes [30]. Figure 1 displays the A_0 and S_0 modes schematically. Lamb waves are dispersive waves and therefore, their velocity varies with the frequency. With the assumption of slowly varying plate thickness, the velocities change either with the frequency or the plate thickness. This can be seen in so-called dispersion curves, which can be obtained with the open-source software 'Dispersion Calculator' [31], as also used in [32].

2.2 Modal parameters of plates

Within structural dynamics, the finite element method serves to predict a structure's vibration behavior in response to dynamic excitation. This method becomes increasingly expensive in terms of computational cost for higher frequencies, as a minimum number of elements per wavelength is necessary for accurate results [33]. The vibrational response across the frequency spectrum may be expressed as a superposition of the structure's modes connected to the respective natural frequencies [34]. Consider the eigenvalue problem resulting from the finite element method as described in the literature [35]. The eigenfrequencies and eigenvectors are the solutions to this eigenvalue problem. Figure 2 shows the mode shape connected to the first natural frequency f_1 of a square plate with free-free boundary conditions on the left and the second mode shape on the right.
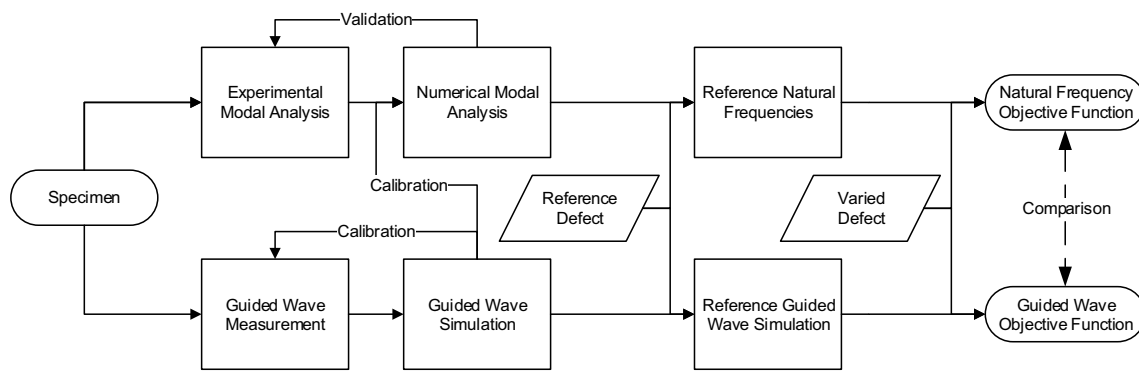
Fig. 3 A diagram encompassing the entire methodical procedure, whose components are described by the following subsections

Table 1 Material parameters of the aluminum plate		
E		67.9 GPa
ρ		2,675 kg m^{-3}
ν		0.277
v_s		3,155 m s^{-1}
v_p		5,682 m s^{-1}

3 Experimental setup and numerical model

This section introduces the investigated specimens with artificial defects (Sect. 3.1). Additionally, the experimental and simulation setups for the measurement of the modal parameters and the guided waves are introduced (Sects. 3.2 and 3.3). Next, the procedures for evaluating the response of guided waves and modal features after changes in the defect parameters are explained in Sect. 3.4. Refer to Fig. 3 for a visual representation of the entire scope of this study.

3.1 Specimens with artificial defects

This study investigates an aluminum plate made of the AlMg3 alloy. The plate is square with a side length of 40 cm and a thickness of 1 cm. The density ρ is calculated by weighing the specimen and measuring its dimensions. Furthermore, the time-of-flight for the p- and s-waves is measured using the OmniScan MX2 ultrasonic device from the company Olympus (Evident) with a 2.25 MHz p-wave transducer (V104-RM) and a 5 MHz s-wave transducer (V157-RM) in a pulse-echo configuration. With the time-of-flight and the measured plate thickness, the longitudinal v_p and transversal v_s ultrasonic wave speeds are calculated. Young's modulus E and Poisson's ratio ν are derived from v_p, v_s, and ρ. The measured and derived material parameters of the plate are given in Table 1.

Using dispersion curves with the material parameters of AlMg3, it can be shown that around 70 kHz, the center frequency of the chosen transducer, the A_0 mode shows large changes in the velocity and is therefore sensitive towards plate thickness changes, see Fig. 4.

This study considers the influence of a defect on the ultrasound signals and modal parameters of the plate. A simple shape makes up the defect, which is described by the four parameters maximum depth D, diameter W, and the position of its center x_d and y_d. This is displayed in Figs. 5 and 6.

The defect depth profile, which is Hann-shaped, is calculated as

$$T(r) = \begin{cases} T_0 - \frac{D}{2}\left[1 + \cos\left(\frac{2\pi r}{W}\right)\right] & r < \frac{W}{2} \\ T_0 & r \geq \frac{W}{2}. \end{cases} \tag{1}$$

Here, T_0 represents the nominal plate thickness and r is the radial coordinate centered at the defect. This function generates a smoothly varying shape. The defect shape is adopted from [29].

Fig. 4 Dispersion curves of the phase and group velocities for the $40 \times 40 \times 1$ cm plate using the aluminum material parameters given in Table 1
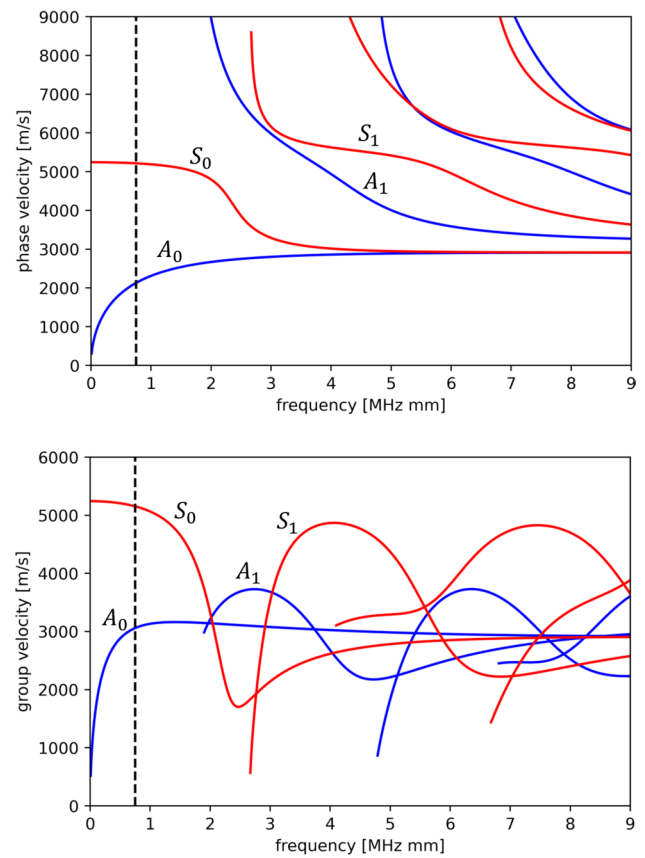

Fig. 5 Plate with defect, where W is the defect diameter at the surface and x_d and y_d mark the position of the circular defect's center
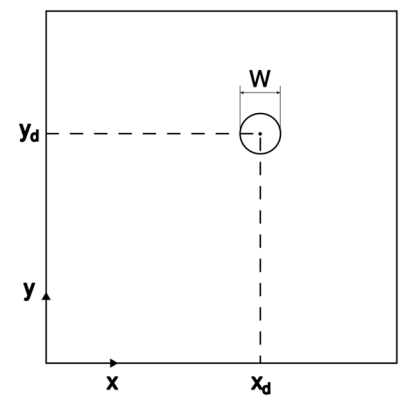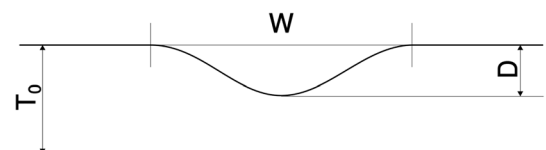

Fig. 6 Plate with defect, where W is the diameter, D represents the maximum depth, and T_0 is the plate thickness

3.2 Measurement setup for guided waves and calibration of the numerical model

To calibrate the guided wave simulations, measurements are conducted with a laser Doppler vibrometer (LDV) with an OFV-505 sensor head and the OFV-5000 controller manufactured by Polytec. The velocity decoder VD-O9 is used. The LDV is mounted on a robot (UR5 by Universal Robots) and pointed orthogonally at the surface of the plate. Therefore, the local particle velocity of the out-of-plane components of the Lamb wave modes is measured. A sine

signal with four bursts at 70 kHz (see Fig. 7) excites the shear wave transducer V151 by Panametrics. A TiePie HS5 generates the waveform. In order to capture the propagation of the Lamb wave in the x- and y-direction relative to the transducer position, several locations for the measurement points are investigated, see Fig. 7. Five measurement positions are staggered in the y-direction with 3 cm increments starting from the transducer. Three further measurement points are staggered in the x-direction using 3 cm increments. The latter corresponds to the horizontal line of measurement points in Fig. 7.

The simulation is conducted with the software Salvus by Mondaic AG [36]. Salvus is based on the spectral element method and is capable of conducting waveform simulations on the GPU. It furthermore offers a meshing routine for changing the topography of the mesh. In our study, a structured mesh is deformed in order to introduce the defect. The excitation wavelet used for the simulation is extracted from a measurement close to the transducer. The transducer is modeled as a point source with forces in the x-, y-, and z-direction. The magnitude of each force is calibrated by an optimization scheme using the Simplex algorithm. As an objective function, the least-square norm $\mathcal{L}$ of the difference between the measured and the simulated signal's waveform is chosen (see Eq. 4). After the optimization of the three forces, a 3.2 times higher force in the x-direction than in the y-direction is identified. Here, the y-direction represents the direction of the polarization of the transducer. The remaining force in the x-direction could be explained by manufacturing inaccuracies of the transducer. With this procedure, the force in the z-direction converges to 0.

We further simulate a B-scan of two 2 m long measurement lines in the x- and y-directions to discern, which wave modes are present in the measured signal. Absorbing boundary conditions are applied to the sides of the plate. The resulting B-scans are given in Fig. 8. The negative slope of the phase fronts relating to the A_0 mode in Fig. 8 may be explained by the comparatively coarse spatial discretization chosen for this simulation. It can be seen that two distinct wave modes are present. By fitting a line through each respective wave mode, the velocities are determined as 3125.0 m s^{-1} and 5115.0 m s^{-1}. The velocities of the A_0 and S_0 modes are 3049.3 m s^{-1} and 5159.2 m s^{-1} based on the analytically determined values (see Fig. 4) and for the center frequency of the wavelet (see Fig. 7). It can be concluded that these modes are the A_0 and S_0 modes since no further modes are present. The A_0 mode is dominant within the signals compared with the S_0 mode, because the A_0 mode exhibits stronger out-of-plane components in comparison with S_0. The modes are fully separated after 30 cm. A major contribution to the superimposed waveform stems from the A_0 mode, whose amplitude is approximately 6 times larger than that of the S_0 mode.
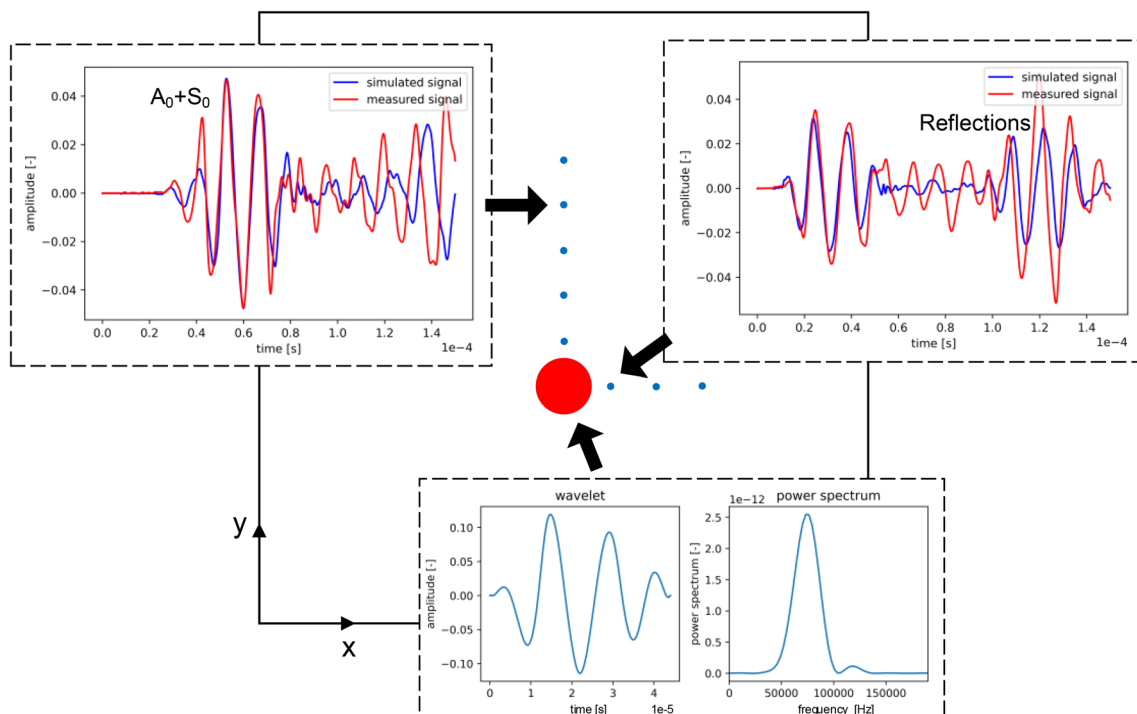

Fig. 7 Experimental setup for calibrating the waveform simulation: the red circle denotes the signal source, while the blue points indicate receiver locations used in the calibration process. For two selected receiver positions, the simulated and corresponding measured signals are shown. Additionally, the excitation waveform or wavelet is provided at the bottom

Fig. 8 A B-scan related to measurement lines in the *x*- and *y*-direction is shown on the left and right, respectively. Absorbing boundary conditions are applied to the plate's sides to eliminate side wall reflections. The color bar is clipped to make the S_0 mode visible
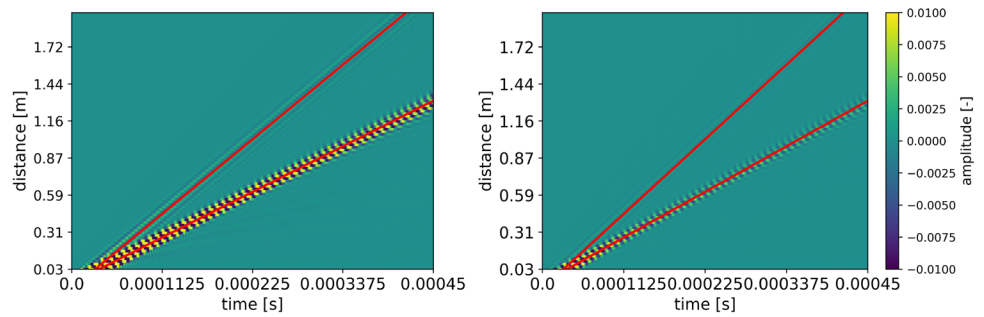
For the subsequent simulations, a denser receiver alignment is applied, leading to a total of 421 receivers. This is displayed in Fig. 9.

3.3 Measurement setup for modal parameters and calibration of the numerical model

Within the experimental modal analysis setup, the plate is suspended on two strings at intervals of thirds aligned in parallel to the plate edges, see Fig. 10. The plate is excited by the SAM Scalable Automatic Modal Hammer at the upper left corner.

Fig. 9 Receiver and source positions on the plate used for evaluation of the objective function for the waveform simulation. The red circle represents the source, and the blue points denote the receiver positions on the plate
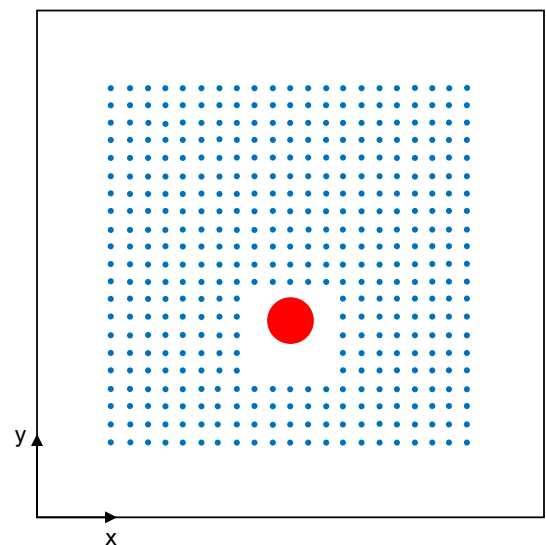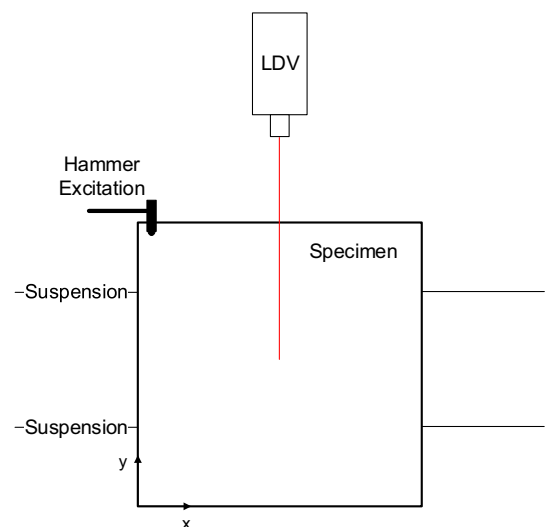
Fig. 10 A depiction of the experimental modal analysis measurement setup. The specimen is suspended by two strings, excited by a modal hammer, and the response is captured by an LDV aligned orthogonally to the surface of the plate

Using a Polytec LDV with a PSV-I-500 scanning head and a PSV-500-3D-H frontend, the structure's velocities in z-direction at the top surface are captured on a regular 15×15 grid. The modal analysis is carried out based on these velocity data using ME'scope for frequencies up to 1,100 Hz. This analysis results in the first natural frequency as 209 Hz.

The considered plate is modeled with the finite element method in COMSOL as a linear three-dimensional volume model with free-free boundary conditions. Quadratic serendipity polynomials serve as the shape functions for the weak form. The geometry is meshed with 1,096 tetrahedral elements yielding 15,405 degrees of freedom for the numerical modal analysis. The maximum element edge length of 2 cm results in at least 10 quadratic elements per wavelength when the first mode shape is considered.

This numerical model's agreement with the measurements is evaluated based on the error ε defined in Eq. (2) with respect to the first natural frequency.

$$\varepsilon = \frac{|f_{\text{num}} - f_{\text{exp}}|}{f_{\text{exp}}} \times 100\% \tag{2}$$

The density, Young's modulus, and Poisson's ratio for the numerical model are set in accordance with the experimentally determined values given in Table 1. Using these material parameters leads to an error of $\varepsilon < 2\%$ in terms of the first natural frequency with respect to the experiment. This parameterization of the simulation model results in a consistent arrangement of the mode shapes in the considered frequency range between the experiment and simulation. The described frequency shift is readily explained by the non-perfect approximation of the ideal boundary conditions by the support chosen for the experimental setup. This is a well-known challenge in the literature; see, for instance, [37].

3.4 Change in guided wave and modal features after defect parameter variation

In this study, the simulation models for the modal and Lamb wave parameters are evaluated as a function of the defect parameters. To achieve this, the four parameters of the defect x_d, y_d, W, and D are varied. For this, two of the four parameters are varied in 51 steps in a full-factorial manner, while the remaining two are kept constant. This is done for all six parameter combinations. The range of the defect parameters' values is given implicitly using the minimal and maximal values in Table 2.

The changes in the system response are investigated with respect to a reference parameterization considered as

$$\mathbf{m}_{\text{ref}} = \begin{Bmatrix} x_{d,\text{ref}} \\ y_{d,\text{ref}} \\ W_{\text{ref}} \\ D_{\text{ref}} \end{Bmatrix}. \tag{3}$$

We formulate the objective function $\mathcal{L}$ in terms of the defect parameter vector $\mathbf{m}$ and the system response vector $\mathbf{q}$ as

$$\mathcal{L}(\mathbf{m}) = ||\mathbf{q} - \mathbf{q}_{\text{ref}}||_2. \tag{4}$$

Here, the response $\mathbf{q}_{\text{ref}}$ corresponds to the defect parameterization $\mathbf{m} = \mathbf{m}_{\text{ref}}$. Now, the optimization procedure aims to solve

$$\mathbf{m} = \arg \min \mathcal{L}(\mathbf{m}). \tag{5}$$

For the Lamb waves, changes in the full waveform and the A_0 group velocity ($\mathcal{L}(\mathbf{m}) = ||v_{A_0} - v_{A_{0,\text{ref}}}||_2$) are investigated.

The group velocity is determined by truncating the signal around the expected arrival time of the A_0 mode and by picking the maximum of the Hilbert envelope [38] of the signal, where the A_0 mode makes up the strongest contribution. This method is referred to as the group velocity method within the remainder of the text. In order to get the velocity,

Table 2 Defect parameter ranges including reference configuration	Parameter	Minimum (cm)	Reference (cm) $\boxtimes_{\text{ref}}$	Maximum (cm)
	x_d	5	$x_{d,\text{ref}} = 20$	35
	y_d	5	$y_{d,\text{ref}} = 20$	35
	W	1	$W_{\text{ref}} = 4.5$	9
	D	0.1	$D_{\text{ref}} = 0.45$	0.9

the determined time point is divided by the distance from the source to the receiver. Further, the Hilbert envelope was smoothed using a Savitzky–Golay filter [39], which does not shift the position of the maximum. The smoothed Hilbert envelope of a signal can be seen in Fig. 11.

For the modal parameters, the first and second eigenfrequencies f_1 and f_2 are investigated individually. Here, $\mathbf{q}_{ref}$ is set to $f_{1,ref}$ and $f_{2,ref}$, respectively.

4 Results and discussion

This section presents the objective function values obtained from the four methods. The objective functions are shown for the six unique pairings of the defect parameters (see Table 2). They are first evaluated separately for the guided wave-based approaches on the one hand, and the natural frequency-based approach on the other hand (Sect. 4.1), and subsequently compared (Sect. 4.2). Note that the results presented in this section stem from computer simulations, and the measurements described in Sect. 3 serve as the initial calibration of the simulation models.

4.1 Evaluation of the objective functions

The objective function results are grouped for pairs of defect parameters. Figure 12 shows the results as a function of the spatial defect coordinates x_d and y_d, and Fig. 13 shows the same results for an off-center reference defect position at $x = 10.49$ cm and $y = 11.86$ cm. Figure 14 depicts the results over varying defect dimensions D and W. The joint effects of x_d with D and x_d with W are displayed by Fig. 15 and Fig. 16, respectively. Figure 17 shows the objective function $\tilde{\mathcal{L}}$ as a function of y_d and D, and finally, Fig. 18 shows it as a function of y_d and W. Each figure contains four graphs, where the top left corresponds to the FWI results and the top right visualizes $\tilde{\mathcal{L}}$ using the group velocity of the A_0 mode. The bottom left and right graphs are connected to the first and second natural frequencies, respectively. The objective functions are normalized to the interval [0, 1] as $\tilde{\mathcal{L}}$. This normalization makes the objective function evaluations qualitatively comparable in terms of measurement noise and error amplitude. Here, an error norm value of 0 indicates no deviation in the data observed from the reference configuration on the one hand and the modified configuration on the other hand. Following Eq. (4), a value of 1 indicates the maximum corresponding deviation.

4.1.1 Guided waves

For the normalized objective function $\tilde{\mathcal{L}}$ surfaces and the variation of the x- and y-position, the full waveform and the group velocity surfaces (Fig. 12 top left and right) show a maximum at the source position. The non-symmetry can be accounted for by using forces in the x- and y-direction for the source. The high objective function values close to the source can be explained on the one hand by the high ultrasound amplitudes in that region. Around the source, the FWI objective function shows rings, which can be explained by the so-called cycle-skipping. The reason for this is that the least squares objective function $\tilde{\mathcal{L}}$ only has a narrow parameter range where it is locally convex with respect to phase shifts in the signal [40]. Other error measures, such as cross-correlation, can mitigate this problem. The FWI $\tilde{\mathcal{L}}$ shows a non-smooth surface with local minima. For this reason, it is not suited for gradient-based optimization

Fig. 11 Procedure for the group velocity method via determining the group velocity of the A_0 mode by picking the time point at the maximum of the Hilbert envelope
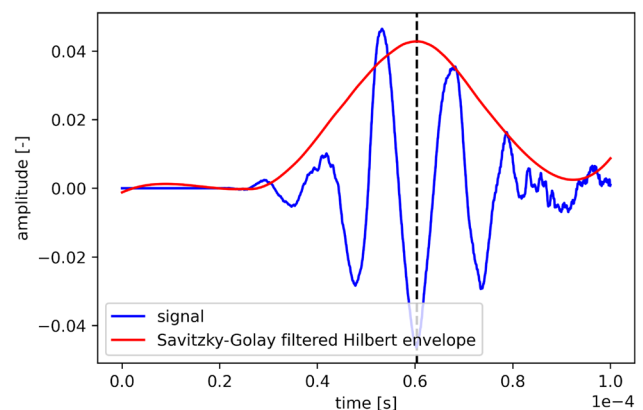
Fig. 12 $\tilde{\mathcal{L}}$ resulting from the reference defect parameters and a variation of its *x*- and *y*-position
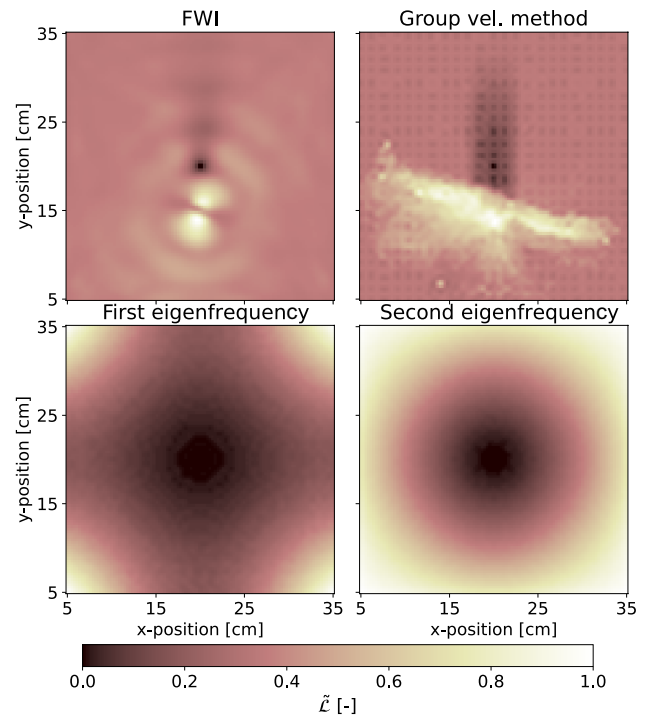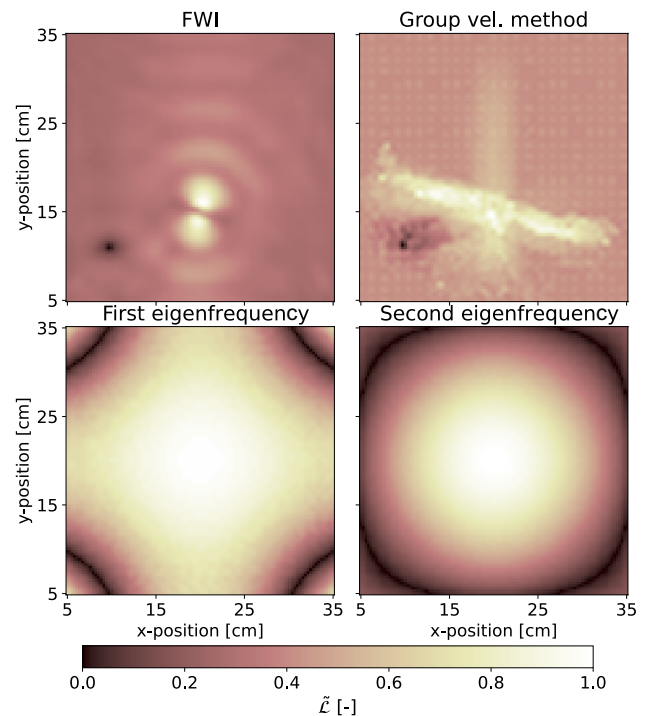

Fig. 13 $\tilde{\mathcal{L}}$ resulting from the reference defect parameters at x = 10.49 cm and y = 11.86 cm and a variation of its *x*- and *y*-position

algorithms or demands that the starting value be close to the true value. The objective function resulting from the A_0 mode shows a large cloud of local minima around the true defect position. With some smoothing within post-processing, this may yield a less steep global minimum. Further, the maximum at the source position is more pronounced in comparison to the FWI error, and at each receiver location, lower errors are reached. These effects around the source remain for the altered reference defect position, see Fig. 13. However, while the minimum connected to

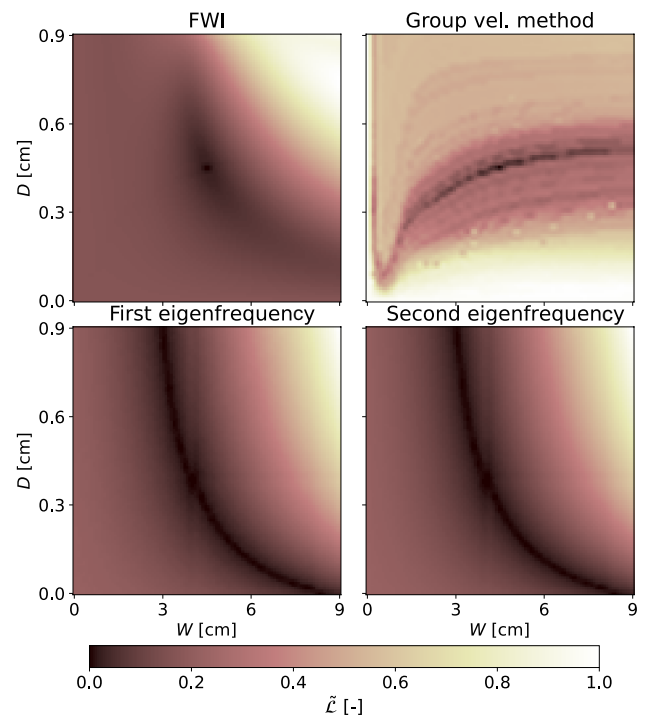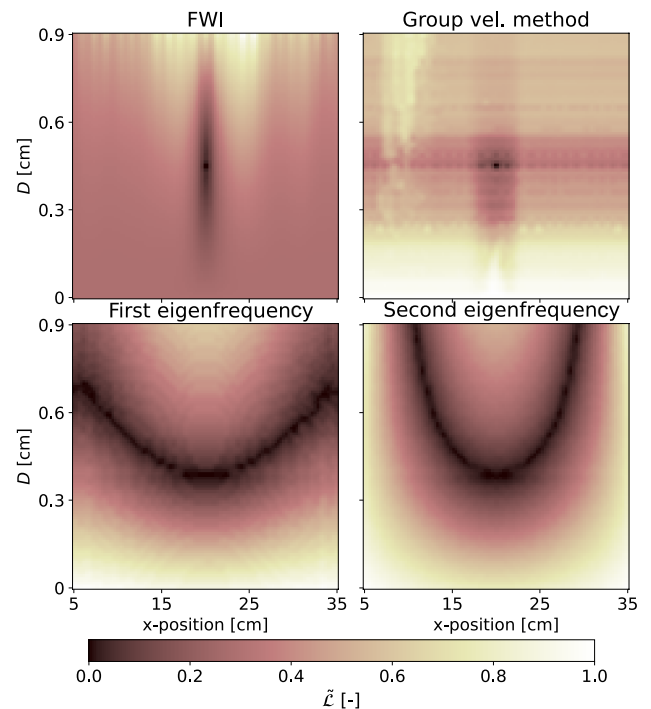**Fig. 14** The figure shows $\tilde{\mathcal{L}}$ for a variation of D and W

Fig. 15 The figure shows $\tilde{\mathcal{L}}$, where D and x_d deviate from the reference configuration

FWI remains equally accurate, the minimum for the off-center defect position is less spread out when compared to the data from the centered position. The deviation of the diameter and maximum depth of the defects show a similar trend for the FWI objective function (see Fig. 14) as for the eigenfrequencies, where the minimum of the FWI error has the smallest area and is, therefore, the least ambiguous. The group velocity of the A_0 mode shows a different behavior. The reason for this can be the different slopes of the S_0 and A_0 modes within the dispersion curves at 70

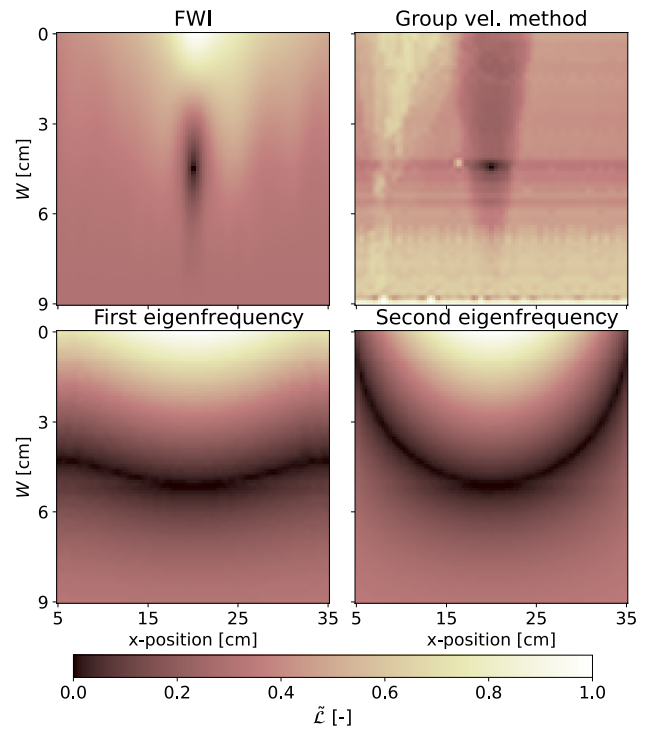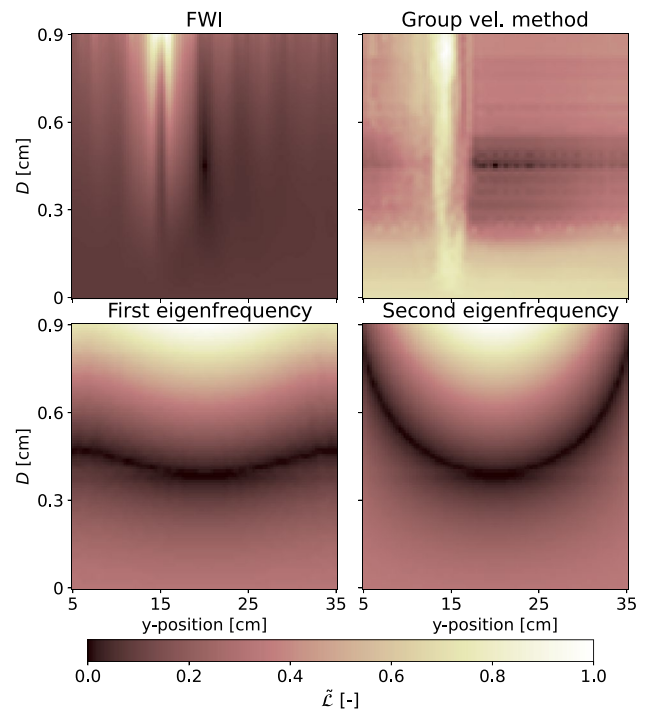**Fig. 16** Here, $\tilde{\mathcal{L}}$ is shown for a variation of x_d and W

Fig. 17 The figure shows $\tilde{\mathcal{L}}$, where D and y_d deviate from the reference configuration

kHz. The A_0 group velocity is picked instead of that related to S_0 because the amplitude of the A_0 mode is significantly higher. Within the FWI $\tilde{\mathcal{L}}$, the S_0 and A_0 modes are included with their phase and group velocity. Through the consideration of all Lamb wave modes, using FWI may suppress some information within the data. When the y-position or the diameter of the defect leads to a defect close to the source, high $\tilde{\mathcal{L}}$ values are present for the group velocity of the A_0 and the FWI objective functions. Note that small errors in the objective functions belonging to the group velocity method are present close to the source position. This is due to the superposition of wave modes. However,

Fig. 18 Here, $\tilde{\mathcal{L}}$ is shown for a variation of y_d and W
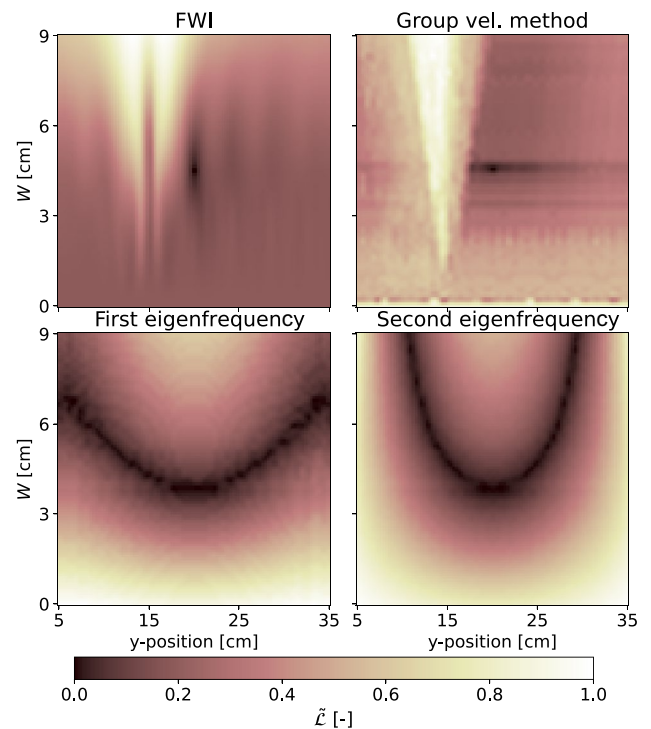
this effect diminishes with growing distance from the source due to the faster velocity and the dominance in terms of the amplitude of the A_0 mode.

4.1.2 Modal

The subplots in the lower left quadrant refer to evaluating Eq. (4) for the first natural frequency, while those in the lower right quadrant are connected to the second natural frequency of the plate. The modal assurance criterion measures the degree of consistency between two vectors, see [41]. It is satisfied for all results, guaranteeing the correct sorting of modes.

Generally, we observe that the objective functions are smooth functions over all four defect parameters. This determines using natural frequency data as suitable when gradient-based optimization algorithms shall be employed.

The first mode shape for an ideal plate without defects, see Fig. 2, is point-symmetric with respect to the plate's center at $\{x, y\} = \{20\,\text{cm}, 20\,\text{cm}\}$. The second mode for an ideal plate without defects is axisymmetric with respect to both $x = 20\,\text{cm}$ and $y = 20\,\text{cm}$. This makes the change in natural frequency with respect to a perturbation in the defect position agnostic to the latter's quadrant within the plate. Axisymmetry of $\tilde{\mathcal{L}}$ with respect to the center lines of the plate is the result of this. In the present case, the error surfaces involving one spatial defect parameter develop single axisymmetry, while the objective function's surface over x_d and y_d shows twofold axisymmetry. To clearly show the latter and the resulting local minima, Fig. 13 is plotted. Our investigations show that neither using linear combinations of several natural frequencies within the objective function nor considering additional, higher natural frequencies can eliminate symmetry problems.

Furthermore, for the centered reference defect and the choice of the first two natural frequencies, all error surfaces show a single global minimum and, thus, the absence of local minima.

Considering the dimensionless gradient of the $\tilde{\mathcal{L}}$ surfaces reveals that the gradient exhibits a stronger sensitivity with respect to the defect position when the second natural frequency is used. This is attributed to the increased number of nodal line crossings in the x and y parameter space.

4.2 Comparison

Table 3 provides a summary of requirements for the measurement setups and the numerical simulations for each method. Additionally, it compares the properties of the resulting objective functions.

Table 3 Advantages and disadvantages of the methods

Criterion	Eigenfrequencies	FWI	Group velocity method
Necessary fidelity of the simulation	Low	High	Low
Necessary measurement point density	Low	High	High
Symmetry problems	Yes	No	No
Gradient around min	Shallow	Steep	Steep
Local minima	No	Yes	Yes

In general, the necessary fidelity of the simulation depends on the size of the defect and on the considered frequency range. However, FWI necessitates the highest measurement fidelity in comparison, as the signal must be represented accurately for time and space coordinates where the wave has been significantly attenuated. When the agreement of the investigated vibration mode can be guaranteed, a single observation point may suffice for the identification of the corresponding eigenfrequency, whereas ultrasound-based procedures rely on dense measurement points.

The minimum for the combined variation of x- and y-position and the diameter or maximum depth is less ambiguous for the Lamb waves than for the eigenfrequencies (see Figs. 15, 16, 17, and 18). Table 4 shows the minimum size relative to the regarded parameter area, determined by applying a threshold of 5% in relation to the respective maximum objective function values. Averaged over the parameter pairings, the minimum size lies in the same order of magnitude for both natural frequencies, while the Lamb wave data leads to minima smaller by orders of magnitude. The minima sizes for FWI and for the group velocity method are generally in the same order of magnitude. However, two irregularly large minima are present for the parameter combinations W and D as well as y and D when using FWI. These outliers lead to the minimum corresponding to the group velocity method objective function having the smallest area and, therefore, being the least ambiguous in this regard.

Further, shallow gradients surround the minimum for the eigenfrequency data. This also holds true when considering the variation of D and W using FWI (see Fig. 14). However, the gradients are steeper when compared to natural frequency data.

Additionally, positioning the reference defect off-center yields perfectly axisymmetric objective functions for natural frequency data, see Fig. 13. The natural frequencies alone do not encode the information to resolve this ambiguity as elaborated in Sect. 4.1. Partially due to the choice of the error norm for the objective function, the Lamb wave objective functions exhibit local minima. Using FWI exhibits less local minima than using the group velocity method does, where these minima mainly occur in proximity to the global minimum, while using the first two natural frequencies produces up to four local minima when the reference defect is not located at the center of the plate.

The influence of environmental conditions on the suitability of modal methods for the purpose of damage detection demands a brief discussion. A homogeneous temperature increment does not influence the mode shapes of a structure. For complex structures such as buildings or bridges, a change in ambient temperature may lead to a heterogeneous temperature field within the structure. The influence of temperature on the efficacy of employing modal methods for damage assessment to large structures has been studied in the literature, see [42]. For simple structures like the presently studied plate, the temperature is straightforward to determine. A change in temperature shifts the natural frequencies due to the temperature dependence of Young's modulus. Assuming an uncertainty in the temperature measurement of ±1 K, the temperature-dependence of the material aluminum, see [43], leads

Table 4 Relative size of the optimum at a threshold of 5% of the maximum objective function value

Parameters	FWI	Group velocity method	f_1	f_2
x & y	0.04	0.05	11.51	4.07
W & D	1.94	0.07	14.03	13.96
x & D	0.08	0.04	7.83	6.63
x & W	0.08	0.08	9.54	10.26
y & D	1.86	0.07	9.57	10.34
y & W	0.16	0.12	7.98	6.64
Mean	0.46	0.07	10.18	8.31

to an uncertainty in the natural frequencies that amounts to two orders of magnitude less than the corresponding influence of the defects investigated in our study. Thus, it is deemed negligible here. The influence of uncertain mounting or boundary conditions remains significant, and the reader is referred to the pertinent literature, see [37].

5 Conclusions

In conclusion,

- The objective functions have been evaluated given the first and second natural frequency, the full waveform, and the group velocity of the A_0 mode.
- The effect of the defect position and geometry on the objective function has been studied.
- Advantages and drawbacks of using each simulation method have been obtained.

Using modal data yields ambiguous, albeit smooth estimates for both the defect position and size. Employing ultrasound methods provides compact objective function minima, but does not produce gradients pertinent to the global minimum when the initial guess for the unknown parameters deviates significantly from their true values. Therefore, we recommend a two-step procedure that begins with using eigenfrequency data and uses these results as the initial vector for an ultrasound procedure. These conclusions apply to the simulated case study with the specified defect and specimen configurations, and generalizations, especially those to equivalent experimental workflows with real transducers, need to be done with a lot of care.

Future research should investigate, whether the natural frequency and ultrasound methods could be employed simultaneously. The latter promises a decrease in solution time. To achieve this, suitable weighting factors for the methods shall be computed. Focusing on the defect's x- and y-position, our data suggest that the local minima produced by, say, FWI could be compensated through the natural frequency objective function's gradient, given an appropriate weighting. Further, the effect of different excitation frequencies on the objective function is an interesting future study. Finally, the effect of using mode shape data instead of natural frequencies should be studied, and different error norms should be investigated.

Author contributions K.-A.H.: conceptualization, methodology, software, validation, formal analysis, investigation, visualization, writing—original draft, writing—review and editing, project administration. S.S.: conceptualization, methodology, software, validation, formal analysis, investigation, data curation, visualization, resources, writing—original draft, writing—review and editing, project administration. J.K.: conceptualization, methodology, software, validation, formal analysis, investigation, writing—review and editing. S.M.: supervision, resources, writing—review and editing. C.U.G.: supervision, resources, writing—review and editing.

Data availability The raw data are available from the corresponding author upon reasonable request.

Code availability The code is available from the corresponding author upon reasonable request.

Declarations

Ethics approval and consent to participate Not applicable.

Consent for publication Not applicable.

Competing interests The authors declare that they have no competing interests.

Discover

References

1. Zielińska M, Rucka M. Imaging of increasing damage in steel plates using lamb waves and ultrasound computed tomography. Materials. 2021;14(17):5114. https://doi.org/10.3390/ma14175114.
2. Krautkrämer J, Krautkrämer H. Ultrasonic testing of materials. Heidelberg: Springer; 1990. https://doi.org/10.1007/978-3-662-10680-8.
3. Zhao X, Royer RL, Owens SE, Rose JL. Ultrasonic lamb wave tomography in structural health monitoring. Smart Mater Struct. 2011;20(10):105002. https://doi.org/10.1088/0964-1726/20/10/105002.
4. Belanger P, Cawley P, Simonetti F. Guided wave diffraction tomography within the born approximation. IEEE Trans Ultrason Ferroelectr Freq Control. 2010;57(6):1405–18. https://doi.org/10.1109/TUFFC.2010.1559.
5. Guy P, Jayet Y, Goujon L. Guided-wave interaction with complex delaminations: application to damage detection in composite structures. In: Smart nondestructive evaluation and health monitoring of structural and biological systems II, vol. 5047, SPIE; 2003. p. 25–33. https://doi.org/10.1117/12.483926.
6. Tan K, Guo N, Wong B, Tui C. Experimental evaluation of delaminations in composite plates by the use of lamb waves. Compos Sci Technol. 1995;53(1):77–84. https://doi.org/10.1016/0266-3538(94)00076-X.
7. Maio L, Hervin F, Fromme P. Guided wave scattering analysis around a circular delamination in a quasi-isotropic fiber-composite laminate. In: Health monitoring of structural and biological systems XIV, vol. 11381. SPIE; 2020. p. 77–83. https://doi.org/10.1117/12.2559125.
8. Huthwaite P. Improving accuracy through density correction in guided wave tomography. Proceed Royal Soci A: Math, Phys Eng Sci. 2016;472(2186):20150832. https://doi.org/10.1098/rspa.2015.0832.
9. He J, Rocha DC, Leser PE, Sava P, Leser WP. Least-squares reverse time migration (lsrtm) for damage imaging using lamb waves. Smart Mater Struct. 2019;28(6):065010. https://doi.org/10.1088/1361-665X/ab14b1.
10. Rao J, Ratassepp M, Fan Z. Guided wave tomography based on full waveform inversion. IEEE Trans Ultrason Ferroelectr Freq Control. 2016;63(5):737–45. https://doi.org/10.1109/TUFFC.2016.2536144.
11. Stache M, Guettler M, Marburg S. A precise non-destructive damage identification technique of long and slender structures based on modal data. J Sound Vib. 2016;365:89–101. https://doi.org/10.1016/j.jsv.2015.12.013.
12. Rus J, Grosse CU. Thickness measurement via local ultrasonic resonance spectroscopy. Ultrasonics. 2021;109:106261. https://doi.org/10.1016/j.ultras.2020.106261.
13. Schneider F, Papaioannou I, Straub D, Winter C, Müller G. Bayesian parameter updating in linear structural dynamics with frequency transformed data using rational surrogate models. Mech Syst Signal Process. 2022;166:108407. https://doi.org/10.1016/j.ymssp.2021.108407.
14. Li Y, Cheng L, Yam L, Wong WO. Identification of damage locations for plate-like structures using damage sensitive indices: strain modal approach. Comput Struct. 2002;80(25):1881–94. https://doi.org/10.1016/S0045-7949(02)00209-2.
15. Tufoi M, Gillich G, Mituletu I, Iancu V. Location of the corrosion damage in rectangular plates. In: 11th International Conference on Damage Assessment of Structures (DAMAS 2015). Journal of Physics: Conference Series, vol. 628. IOP Publishing; 2015. p. 012005. https://doi.org/10.1088/1742-6596/628/1/012005.
16. Le T-C, Ho D-D, Nguyen C-T, Huynh T-C. Structural damage localization in plates using global and local modal strain energy method. Adv Civil Eng. 2022;2022:4456439. https://doi.org/10.1155/2022/4456439.
17. Hou J, Jankowski Ł, Ou J. Structural health monitoring based on combined structural global and local frequencies. Math Probl Eng. 2014;2014:405784. https://doi.org/10.1155/2014/405784.
18. Park J-H, Kim J-T, Hong D-S, Mascarenas D, Peter Lynch J. Autonomous smart sensor nodes for global and local damage detection of prestressed concrete bridges based on accelerations and impedance measurements. Smart Struct Syst. 2010;6(5–6):711–30. https://doi.org/10.12989/sss.2010.6.5_6.711.
19. Sun XD, Sun XY, He J, Hou GL. Bayesian-based structural damage detection on the integration of global and local information. Adv Struct Eng. 2015;18(4):543–53. https://doi.org/10.1260/1369-4332.18.4.543.
20. Mehrez L, Doostan A, Moens D, Vandepitte D. Stochastic identification of composite material properties from limited experimental databases, part ii: Uncertainty modelling. Mech Syst Signal Process. 2012;27:484–98. https://doi.org/10.1016/j.ymssp.2011.09.001.
21. Debruyne S, Vandepitte D, Moens D. Identification of design parameter variability of honeycomb sandwich beams from a study of limited available experimental dynamic structural response data. Comput Struct. 2015;146:197–213. https://doi.org/10.1016/j.compstruc.2013.09.004.
22. Batou A, Soize C. Stochastic modeling and identification of an uncertain computational dynamical model with random fields properties and model uncertainties. Arch Appl Mech. 2013;83:831–48. https://doi.org/10.1007/s00419-012-0720-7.
23. Mengelkamp G, Fritzen C-P. Combination of global and local methods for structural health monitoring. In: 24th Conference and Exposition on Structural Dynamics 2006, IMAC-XXIV. Springer Nature; 2006.
24. Fritzen C-P, Mengelkamp G. In-situ damage detection and localisation in stiffened structures. In: 23rd Conference and Exposition on Structural Dynamics 2005, IMAC-XXIII. Springer Nature; 2005.
25. Wang Y, Hao H. Damage identification of steel beams using local and global methods. Adv Struct Eng. 2012;15(5):807–24. https://doi.org/10.1260/1369-4332.15.5.
26. Yan F, Rose JL. Defect detection using a new ultrasonic guided wave modal analysis technique (umat). In: Health monitoring of structural and biological systems 2010, vol. 7650. SPIE; 2010. p. 240–248. https://doi.org/10.1117/12.847674
27. Ahmed S, Zhou P, Zager S, Kopsaftopoulos F. Local and global structural health monitoring via stochastic functional time series methods: a critical assessment and comparison; 2022. https://doi.org/10.2514/6.2022-4001.
28. Harb M, Yuan F. Non-contact ultrasonic technique for lamb wave characterization in composite plates. Ultrasonics. 2016;64:162–9. https://doi.org/10.1016/j.ultras.2015.08.011.
29. Huthwaite P. Evaluation of inversion approaches for guided wave thickness mapping. Proceed Royal Soci A: Math, Phys Eng Sci. 2014;470(2166):20140063. https://doi.org/10.1098/rspa.2014.0063.
30. Auld B. A: Acoustic fields and waves in solids. Malabar: Krieger Publishing Company; 1990.

31. Huber A. Dispersion calculator. Technical report, Deutsches Zentrum für Luft- und Raumfahrt, Augsburg; 2018. https://elib.dlr.de/124561/.
32. Huber A, Sause M. Classification of solutions for guided waves in anisotropic composites with large numbers of layers. J Acoust Soci Am. 2018;144(6):3236–51. https://doi.org/10.1121/1.5082299.
33. Langer P, Maeder M, Guist C, Krause M, Marburg S. More than six elements per wavelength: The practical use of structural finite element models and their accuracy in comparison with experimental results. J Comput Acoust. 2017;25(04):1750025. https://doi.org/10.1142/S0218396X17500254.
34. Ewins DJ. Modal testing: theory, practice and application. Philadelphia: Research Studies Press; 2009.
35. Bertolini AF. Review of eigensolution procedures for linear dynamic finite element analysis. Appl Mech Rev. 1998;10(1115/1):3098994.
36. Afanasiev M, Boehm C, van Driel M, Krischer L, Rietmann M, May DA, Knepley MG, Fichtner A. Modular and flexible spectral-element waveform modelling in two and three dimensions. Geophys J Int. 2019;216(3):1675–92. https://doi.org/10.1093/gji/ggy469.
37. Pavić G. Structure-borne energy flow. In: Crocker MJ, editor. Handbook of noise and vibration control. Hoboken, NJ: Wiley; 2007. p. 232–40. https://doi.org/10.1002/9780470172520.CH74.
38. Ulrich T. Envelope calculation from the hilbert transform. Technical report, Los Alamos National Laboratory, Los Alamos; 2006.
39. Savitzky A, Golay MJ. Smoothing and differentiation of data by simplified least squares procedures. Anal Chem. 1964;36(8):1627–39. https://doi.org/10.1021/ac60214a047.
40. Boehm C, Krischer L, Ulrich I, Marty P, Afanasiev M, Fichtner A. Using optimal transport to mitigate cycle-skipping in ultrasound computed tomography. Medical Imaging 2022: ultrasonic imaging and tomography. 2022;12038:48–57. https://doi.org/10.1117/12.2605894. SPIE.
41. Allemang RJ. The modal assurance criterion (mac): twenty years of use and abuse. In: IMAC-XX (Los Angeles CA, 4-7 February 2002) vol. 1. SPIE; 2002. p. 397–405. http://pascal-francis.inist.fr/vibad/index.php?action=getRecordDetail &idt=14180753.
42. Luo J, Huang M, Lei Y. Temperature effect on vibration properties and vibration-based damage identification of bridge structures: A literature review. Buildings. 2022;12(8):1209. https://doi.org/10.3390/buildings12081209.
43. Hopkins DC, Baltis T, Pitaress JM, Hazelmyer DR. Extreme thermal transient stress analysis with pre-stress in a metal matrix composite power package. Additional papers and presentations (HITEC); 2012. p. 000361–000372. https://doi.org/10.4071/HITEC-2012-THA25.

Publisher's Note Springer Nature remains neutral with regard to jurisdictional claims in published maps and institutional affiliations.

Discover